50 YEARS of strain
strain
An International Journal for Experimental Mechanics

Strain and Displacement Controls by Fibre Bragg Grating and Digital Image Correlation

J. Waldbjørn*, J. Høgh†, J. Wittrup-Schmidt*, M. W. Nielsen‡, K. Branner§, H. Stang* and C. Berggreen†

*Department of Civil Engineering, Technical University of Denmark, Brovej Building 118, 2800, Kgs. Lyngby, Denmark
†Department of Mechanical Engineering, Technical University of Denmark, Nils Koppels Alle, Building 403, 2800, Kgs. Lyngby, Denmark
‡Department of Mechanical Engineering, Technical University of Denmark, Produktionstorvet Building 425, 2800, Kgs. Lyngby, Denmark
§Department of Wind Energy, Technical University of Denmark, Frederiksborgvej 399, 4000 Roskilde, Denmark

ABSTRACT: Test control is traditionally performed by a feedback signal from a displacement transducer or force gauge positioned inside the actuator of a test machine. For highly compliant test rigs, this is a problem since the response of the rig influences the results. It is therefore beneficial to control the test based on measurements performed directly on the test specimen. In this paper, fibre Bragg grating (FBG) and Digital Image Correlation (DIC) are used to control a test. The FBG sensors offer the possibility of measuring strains inside the specimen, while the DIC system measures strains and displacement on the surface of the specimen. In this paper, a three-point bending test is used to demonstrate the functionality of a control loop, where the FBG and DIC signals are used as control channels. The FBG strain control was capable of controlling the test within an error tolerance of 20 $\mu m\,m^{-1}$. However, the measurement uncertainty offered by the FBG system allowed a tolerance of 8.3 $\mu m\,m^{-1}$. The DIC displacement control proved capable of controlling the displacement within an accuracy of 0.01 mm.

KEY WORDS: *digital image correlation, displacement control, fibre Bragg grating, fibre reinforced plastic, three-point bending*

Introduction

Mechanical testing is commonly controlled by a proportional-integral-derivative (PID) controller using the feedback signal from a load cell or a gauge positioned in the actuator of the testing machine e.g. linear variable differential transducer (LVDT). However, the compliance of the load train will in this case affect the results, and it is therefore more accurate to control the test by measurements performed directly on the specimen e.g. by a clip gauge [1], where the strain from the gauge is fed into the PID control loop as an analogue signal. Other measurement techniques have also been used to control tests e.g. digital image correlation [2]. In these efforts, the signal from the external measurements has not been used in the PID controller, instead, an outer control loop was designed to correct the displacement/strain applied by the PID controller in the inner control loop. These methods might be useful when testing specimens with complex geometry and/or test rigs with joints and bearings. In such cases, the desired strain state is not easily obtained, since the displacement measured by the LVDT at the actuator is not the same as the displacement in the specimen, and it is therefore possible to obtain higher accuracy if measurements are performed directly on the specimen and feed into the control loop. The effect of the compliance of the load train is thereby omitted.

FBG sensors are gauges inside optical fibres capable of measuring strains by changes in a reflected light beam. Due to the small diameter and environmental robustness of the fibre optic sensor, it can be embedded into several types of materials e.g. laminated/sandwich composites and concrete, without affecting the mechanical properties [3] of the test specimen. This has made the FBG technology widespread within the field of mechanical engineering covering manufacturing techniques, material/component testing, structural health monitoring (SHM) and damage assessment and support control systems. By embedding/attaching FBG sensors to a structure during manufacturing, it is possible to monitor the process-induced temperature and residual strains as they develop [4–6]. Within material/component testing, the FBG sensor provides accurate and local measurement capabilities of internal stress distribution, stress concentrations and vibrations [7, 8]. Furthermore, FBG sensors can detect cracks and delamination, which are key information in glass fibre reinforced polymer (GFRP) testing [9, 10]. Also, in SHM, the FBG sensors are used for the observation of the in-service structural performance due to ageing and degradation caused by the environment. In this case, the sensors can be used to monitor the integrity of the structure [11–15]. The environmental robustness and high resolution of the FBG sensors enable high precision control suitable for systems in which geometry or harsh environmental conditions do not allow the use of other sensor technologies [16]. When performing tests where a certain strain state is difficult to obtain due to a complex test rig/geometry, it is beneficial to use FBG sensors for control, since they can measure strains directly on the specimen or even inside.

DIC is a technique capable of calculating strains and displacement on a surface on the basis of digital images. Within the field of mechanical and civil engineering, the DIC technology is widespread within multiple categories e.g. material characterization (Young's modulus, Poisson's

doi: 10.1111/str.12089

ratio, elasto-plastic behaviour, etc.), component testing, fracture mechanics and high speed testing for dynamic and high strain rate measurements. With the ability to identify both local and global strain distribution and perform measurements in the plastic regime, the DIC technology has proven to be a useful tool within material testing [17–20]. The DIC technique inherently has no limit of size, and it has been applied for varying length scales covering a few square millimetres up to multiple square metres [21–23]. In fracture mechanics, the DIC technique is able to deliver information about crack propagation, which can be used for the determination of important fracture mechanic parameters [24, 25]. The DIC technique has the ability of high rate image acquisition, which makes it suitable for dynamic measurements [26–28] or even blast tests where it has been used for image acquisition in the range of megahertz [29]. The DIC system is capable of delivering high resolution 3D full field measurements, which are easily integrated in the testing environment. When dealing with a complex specimen geometry and/or load train, the measurement technique represents a substitute to a large number of analogue gauges including extensometers, potentiometers and strain gauges. Thus, with the aim of performing real-time measurements from multiple positions on the test object surface, the DIC technique is implemented in this work for static displacement control.

This paper documents a series of three-point bending tests controlled by a feedback signal acquired from the test specimen by DIC and FBG measurements for displacement and strain controls, respectively. This is performed by a control loop that operates and acquires data from a test station, FBG interrogation system and DIC system. The displacement is applied by the test station using a servo-hydraulic actuator operated by a PID controller. The FBG measurements are obtained by emitting light through two optical fibres, each containing three FBG sensors. The optical fibres are embedded into the GFRP beams during manufacturing, one at the top and one at the bottom of the beam. The reflected light is analysed by an interrogator and converted to strain. The DIC measurements are performed by a stereoscopic camera system, capable of tracking the displacement of the specimen surface by image matching and photogrammetry. The experiments are performed within the linear elastic regime for five GFRP beams with a predefined error tolerance to document the functionality of the control loop.

Principle of Fibre Bragg Grating

An FBG is a short segment of several thousand organised layers with varying refractive indices written into a single mode fibre. When a broad band light beam strikes the interface between each layer in the FBG, the light is reflected and refracted cf. Fresnel equation [29]. When the grating period is equal to the wavelength, each single interface reflection is reflected in the phase magnifying the energy level by positive interference forming a narrow band spectral peak. The remaining reflected spectra are out of the phase with the grating period and therefore erased. By straining the FBG, a shift of the peak reflectivity is generated as illustrated in Figure 1, which is convertible to multiple physical quantities including strain, temperature and vibrations. [30].

Knowing the initial wavelength λ_0, the wavelength change $\Delta\lambda$ and the temperature change ΔT of the specimen, the strain is calculated from Equation (1).

$$\frac{\Delta\lambda}{\lambda_0} = \varepsilon k_\varepsilon + k_t \Delta \mathrm{T} \tag{1}$$

where the gauge factors k_ε and k_t are provided by the FBG manufacturer. The identification of the narrow band light reflected by the FBG is performed by an interrogation monitor, which converts the incident light to an array of discrete digital intensity data.

Principal of Digital Image Correlation

The DIC technique is a non-contact, full field measurement method based on grey-value digital images [31]. The system has two imaging sensors tracking the shape, motion and displacement of an object surface in three dimensions [27]. Figure 2 illustrates a DIC setup with a commercial system, capable of acquiring images of the specimen surface, which are subsequently analysed by the DIC software, [32].

DIC utilise two techniques to acquire data: image matching and photogrammetry [31]. Image matching identifies the position of each measurement point in the two camera images. This is done by dividing the first camera image into squared facets containing multiple pixels. For each facet, a suitable transformation matching the homologous area in the second camera image is derived tracking each successive image with sub-pixel accuracy. The surface must have a stochastic speckle pattern in order

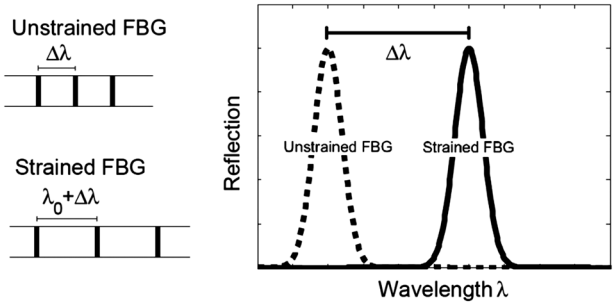

Figure 1: The change in peak reflectivity as a function of the grating period

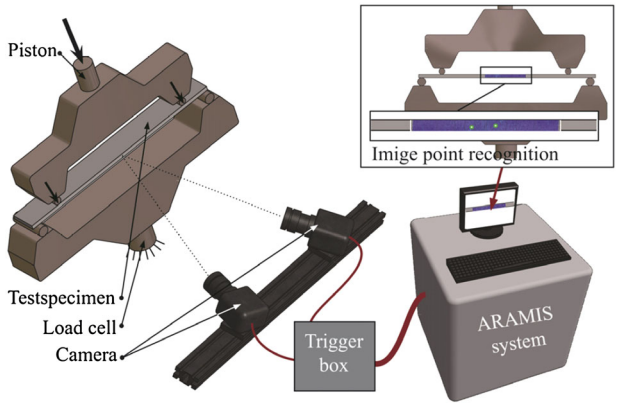

Figure 2: A four-point bending test with the commercial DIC system; ARAMIS

for the facets to be uniquely identifiable. Photogrammetry performs a transformation between the geometric properties of the measurement surface in the photographic image. This technique relies on a calibration to determine the imaging parameters for each camera (intrinsic) and the relative position and orientation of the cameras with respect to each other (extrinsic) [32]. The outcome is a 3D full field component shape and surface displacement field, along with the components of a plane strain tensor.

Test Setup

The test specimen is loaded in a four-column MTS 810 test machine with a T-slot strong table and an axial servo-hydraulic actuator with a static stroke of ±33.00 mm. The servo-hydraulic actuator is an MTS model 244.22 with a load capacity of 100 kN. The oil flow through the actuator is controlled by an MTS servo valve, model 252.24C-04 with a capacity of 38 L min^{-1}. Two feedback transducers are mounted in conjunction with the actuator: an internal LVDT and a load cell model MTS 661.19E-04 with a capacity of 25 kN. The actuator is operated, and the transducer signal is acquired by an MTS FlexTest60 PID controller. The loading nose and support rollers are 40 and 25 mm in diameter, respectively, cf. Figure 3, and the support rollers are able to move horizontally. Electrical resistance strain gauges are mounted on the specimens of the type SR-4 general purpose strain gauges from Vishay Micro-Measurements. The gauge resistance is 120.0Ω ± 0.3% and gauge length 6.99 mm for all specimens, while the gauge factor is 2.075 ± 0.5% for beams 1 and 3 and 2.035 ± 0.5% for the remaining. The optical fibres embedded in the specimens are silica fibres provided by FOS&S. Each fibre contains three draw tower gratings (FBG sensors) with a gauge length of 4.00 mm and an Ormocer coating (cladding diameter of 125 μm). The sensitivity coefficients k_ε and k_T are equal to 7.75E-7 μm m^{-1} and 6.27E-6 K^{-1}, respectively. The signal is acquired by a stand-alone interrogator type: I-MON 512 E-USB with a wavelength range of 1510–1595 nm cf. [33]. The surface is painted with a stochastic black speckle pattern on a white background, and three measurements points (MP) are selected, cf. Figure 3. The displacement of the measurement points is tracked by the commercial DIC system of the type ARAMIS from the company Geseltshaft für Optische Messtechnik (GOM). The camera resolution is 4 megapixels (2352 × 1728 pixels) with 20 mm focal length Titanar lenses. The images are divided into facets of 15 × 15 pixels, with a shift of 13 pixels. The cameras were calibrated to an intersection deviation of 0.024 pixels, with a 250 × 200 mm ARAMIS calibration panel to obtain a measurement area of 330 mm width and 330 mm height. The accuracy of the DIC setup is evaluated by a micrometre of the type: Mitutoyo — series 164 and range 0–50 mm. The micrometre offers an accuracy and resolution

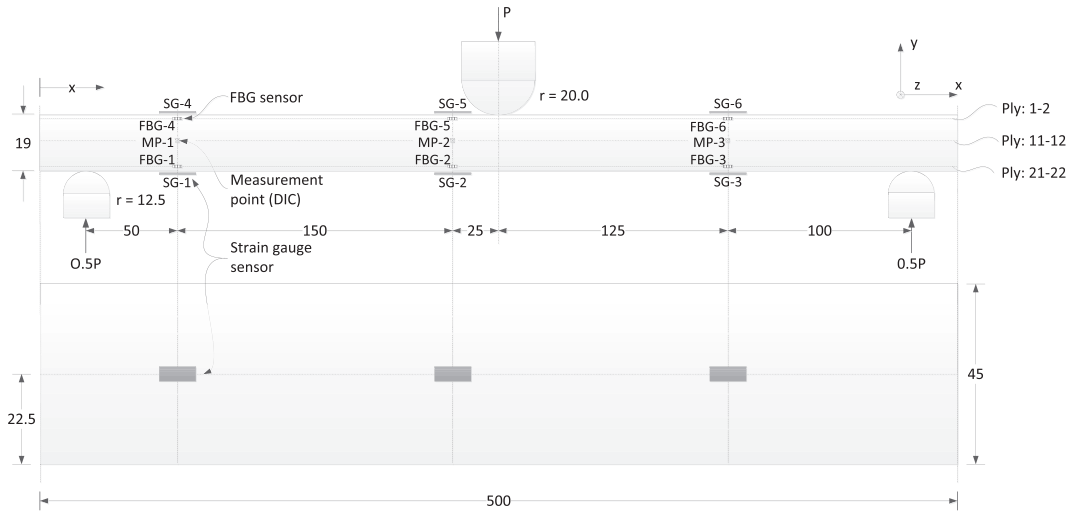

Figure 3: Dimensions of the test setup and specimen along with numbering and location of various sensors

© 2014 Wiley Publishing Ltd | ***Strain*** (2014) **50**, 262–273
doi: 10.1111/str.12089

of 3 μm and ±1 μm, respectively, and is mounted to a linear motion system type: THK-RSR7W. The dimensions of the three-point bending setup and test specimen along with numbering of the FBG sensors, electrical resistance strain gauges and the DIC measurement points (MPs) are displayed in Figure 3.

The entire test setup, with the specimen inserted into the three-point bending rig with the mounted gauges, is presented in Figure 4.

Specimen properties

The test specimen is a GFRP beam with 22 plies of uni-directional (UD) fibre mats of the type L1200/G50F-E06-A, from Devold AMT, with a nominal area weight of 1246 g m^{-2}. The matrix is a thermoset epoxy resin of the type Airstone 760E mixed with Airstone 776H hardener, from Dow Chemicals Company. Five GFRP beams were produced by vacuum infusion with a fibre orientation in the *x*-direction (see Figure 3) and fibre volume fraction of 55% [34]. The stiffness and strength properties of the beams are calculated by the rule-of-mixture on the basis of UD mechanical properties listed in Table 1 [35].

The load capacity at first ply failure (FPF) is estimated on the basis of the max stress failure criterion [35]. This yields a corresponding force of $F_{FPF} = 8.00$ kN. The Young's modulus of the specimen has been determined experimentally to 40.21 GPa.

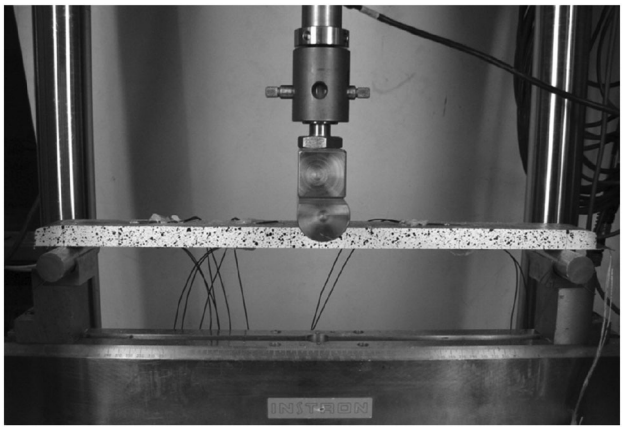

Figure 4: The three-point bending setup with a GFRP beam applied strain gauges, speckle pattern and FBG sensors

Control Loop

The control loop enables static displacement control operated by a feedback signal acquired from the test specimen using DIC or FBG measurements. This control system follows the architecture of a single input-single output feedback control loop [36]. This test configuration is implemented in LabVIEW 8.6, and the implemented test algorithm includes two independent systems: the displacement controlled actuator and the external data acquisition (DAQ) system. The displacement controlled hydraulic actuator is operated through an MTS FlexTest 60 servo controller [37] by the TCP/IP port using a dynamic link library (DLL) [38]. The external DAQ system includes the DIC and FBG measurements. The control loop is executed in a state-machine framework [39] according to the flowchart illustrated in Figure 5.

The control loop is initiated by feeding a displacement input to the servo controller (1) operated by a feedback signal from the LVDT in the actuator. In (2), the actuator is moved towards the end level in a monotonic motion with a predefined time rate. When the defined displacement is reached, the data from the servo controller: LVDT and load cell signals along with the external measurements: FBG and DIC are acquired by (3) and (4), respectively. The displacement input is compared with the response of the specimen, and a deviation is derived. If the deviation is within the error tolerance, the control loop is ready to receive the next user defined displacement input in (6). If the deviation exceeds the error tolerance, the actuator is moved in the direction necessary to reduce the error with a magnitude equal to the deviation. This is carried out by repeating the entire loop from (1) – (5) until a deviation below the error tolerance is obtained.

FBG system—control loop communication

A real-time communication between the I-MON 512E interrogator and the LabVIEW is established through the USB port by a dynamic link library (DLL) [40]. These DLL files are implemented directly in the LabVIEW environment, while all the data analyses are hard-coded in the LabVIEW according to [41]. The functions in the control sequence are presented in a flow chart diagram in Figure 6.

In Figure 6, the communication is initiated in (1), which identifies and configures a communication between the LabVIEW and the I-MON interrogator. The data are collected in a block mode setup separated in three tasks: acquire a single image, convert the analogue signal to an

Table 1: Mechanical properties of a UD-glass fibre ply

E_1 (GPa)	E_2 (GPa)	G_{12} (GPa)	υ_{12} (−)	$\hat{\sigma}_{1t}$ (MPa)	$\hat{\sigma}_{1c}$ (MPa)	$\hat{\sigma}_{2t}$ (MPa)	$\hat{\sigma}_{2c}$ (MPa)	$\hat{\tau}_{12}$ (MPa)
40	9.8	2.8	0.3	1100	600	20	140	70

doi: 10.1111/str.12089

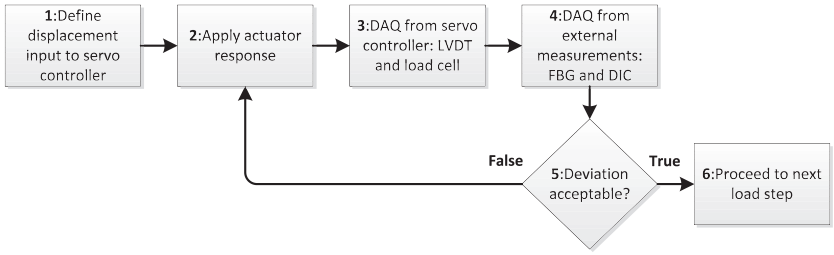

Figure 5: Control loop algorithm operating and acquiring data from servo controller, FBG interrogator and DIC system

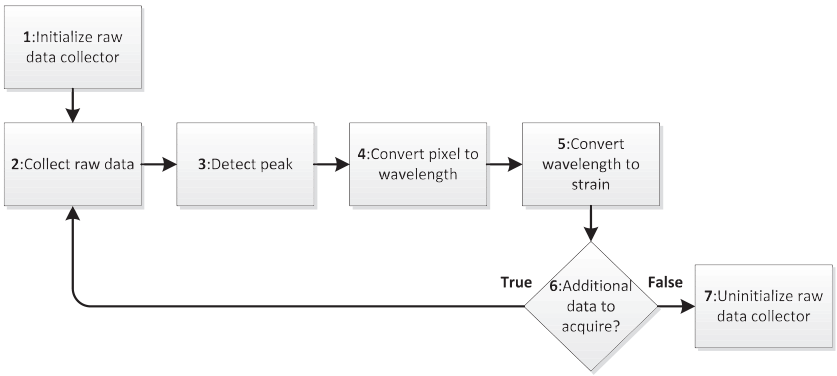

Figure 6: Communication procedure between control loop algorithm and FBG interrogator

array of discrete intensity data and transfer the data from the PCB buffer to the LabVIEW software. The data acquisition is performed in (2) with a predefined cycle time for each iteration. The photoelectrical signal is generated by the linear image sensor consisting of 512 elements. Each element represents one pixel in the image sensor, while the appertaining integer describes the individual pixel response generated by the incident light. The locations of the pixels representing the reflection peak, generated by the reflection spectra of the multitude FBG sensors, are identified in (3). The function pinpoints the individual pixels exceeding the pixel response, defined by a threshold parameter. By a Gaussian fit routine, the location of the peak is determined by including a predefined number of neighbouring pixels in the analysis. In (4), the relation between the pixels on the linear image sensor and the optical wavelength is described by a fifth degree polynomial [33]. A compensation for temperature drift in the interrogator is included by a correction equation [33]. All calibration coefficients are acquired through the USB port from the electronically erasable programmable read-only memory (EEPROM). The relation between the wavelength and strain, present in each FBG included in the system, is outlined in (5) cf. Equation (1). If no additional measurements from the I-MON interrogator are required (6), the programme is stopped (7). This is done by releasing the main PCB internal image data buffer, USB camera, and finally, the USB device and DLL.

Strain control by FBG

The FBG strain control is performed by using strain data from the FBG sensors to obtain an equivalent displacement at the loading point. This is inserted as a displacement input in the control loop cf. Figure 5. The strains at the location of the FBG sensors are converted to a displacement by Bernoulli–Euler beam theory, Navier's stress relation and Hooke's law.

$$\frac{d^2u}{dx^2} = -\frac{M}{EI}z, \qquad \sigma = \frac{M}{I}z, \qquad \sigma = E\varepsilon \tag{2}$$

This yields two relations between displacement and strain for the three-point bending load case

$$u_{max} = \frac{1}{24}\frac{L^3\varepsilon(x)}{xz} \text{ for } x \leq \frac{L}{2} \tag{3}$$

$$u_{max} = \frac{1}{24}\frac{L^3\varepsilon(x)}{(L-x)z} \text{ for } x \geq \frac{L}{2} \tag{4}$$

where x is the position in the x-direction cf. Figure 3, u_{max} is the deflection at centre position, L is the length between the support points, z is the distance from the neutral axis to the FBG sensors in the y-direction and $\varepsilon(x)$ is the strain in the x-direction at the position x. The displacement input at the loading point is derived as the average deflection of all six FBG sensors embedded in the specimen cf. Figure 3.

doi: 10.1111/str.12089

DIC system—control loop communication

The GOM IVIEW software is an extension to the ARAMIS measurement system capable of acquiring single measurement points on the specimen surface in real time [17]. From each measurement point, the 3D coordinates are obtained and fed to the LabVIEW program through a TCP/IP connection. The TCP/IP communication and image processing, performed by IVIEW, is handled in a Python macro with commands from the GOM package [42]. The steps in the communication between the two systems are presented by the flowchart in Figure 7.

In Figure 7, the communication between LabVIEW and DIC is initiated by opening a TCP/IP port in (1). When this communication is established and verified, the LabVIEW application sends a trigger signal to (2) initiating the image acquisition with a predefined frame rate. The coordinates for each measurement point are calculated real time and fed to an internal image buffer. LabVIEW is requesting image data in (3) by generating a trigger signal. This trigger signal is fed through the TCP/IP connection to (4) transferring the data stored in the buffer to (5). When all the data are transferred, the image data buffer is overwritten with new image data while waiting for the next trigger signal by (3). When all the requested data are acquired and the LabVIEW application is terminated, the TCP/IP connection is closed by (7).

Displacement control by DIC

DIC displacement control is carried out using the displacement signals from the measurement points on the surface, cf. Figure 3, to obtain an equivalent displacement at the loading point. These data are inserted as a displacement input for the control loop cf. Figure 5. The relation between the maximum displacement and displacement at a given coordinate x is again derived from the Bernoulli–Euler beam theory.

$$u_{max} = \frac{u(x)}{3\left(\frac{x}{L} - \frac{4}{3}\left(\frac{x}{L}\right)^3\right)} \quad for\ x \leq \frac{L}{2} \tag{5}$$

$$u_{max} = \frac{u(x)}{4\left(\left(1 - \frac{x}{L}\right)\left(\frac{2x}{L} - \frac{1}{4} - \left(\frac{x}{L}\right)^2\right)\right)} \quad for\ x \geq \frac{L}{2} \tag{6}$$

where $u(x)$ is the displacement in the y-direction at position x. The displacement input is obtained by averaging the u_{max} calculated from each of the three measurement points.

Results

A GFRP specimen is tested within the linear elastic regime in a three-point bending rig cf. Figure 4 with a ramped displacement rate of $1\,\mathrm{mm\,s^{-1}}$. The setup is operated by a feedback signal from the test specimen by using FBG and DIC measurements for static strain and displacement control, respectively.

FBG sensor strain control

Static strain control by FBG is utilised to limit the deviation between the displacement input and FBG measurements, within a given error tolerance. The magnitude of this tolerance is given on the basis of the measurement uncertainty and repeatability [43] offered by the FBG system. The repeatability has a standard uncertainty of $0.0994\,\mu\mathrm{m\,m^{-1}}$ from a sample of 160 measurements for each FBG, acquired under constant conditions with a frequency of 970 Hz. The stand-alone interrogation monitor measures wavelengths with an accuracy of ±10 pm cf. [33], which corresponds to $\pm 8.3\,\mu\mathrm{m\,m^{-1}}$ cf. Equation (1). The error tolerance is defined to $\pm 20\,\mu\mathrm{m\,m^{-1}}$, which is equal to approx. ±0.69% of the peak strain, cf. Figure 8. A displacement input with a triangular waveform is applied including 91 iterations forming five peaks. The peak-to-peak amplitude of the displacement input is $2900\,\mu\mathrm{m\,m^{-1}}$ between plies 21–22 at the loading point, see Figure 3. The displacement input is validated by FBG measurements,

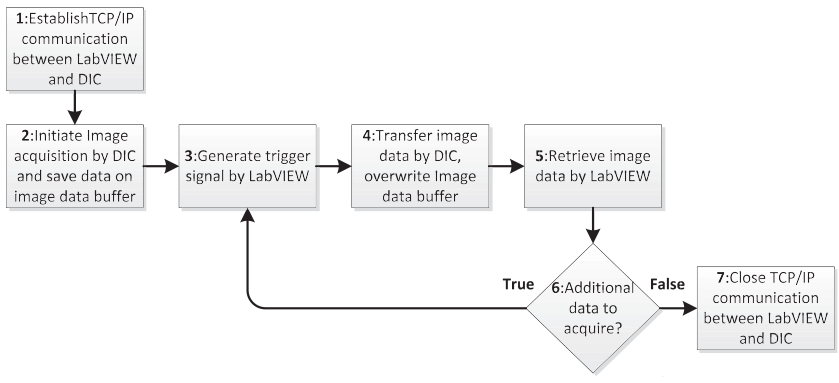

Figure 7: Communication procedure between: control loop algorithm and DIC system

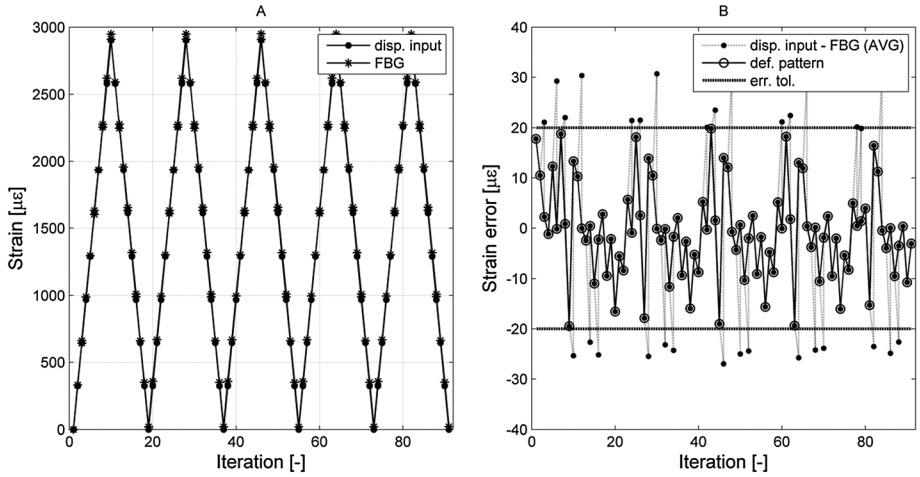

Figure 8: Strain control by FBG (A) displacement input and FBG and (B) discrepancy between displacement input and FBG

which are calculated by converting the strain data from each FBG sensor to obtain an equivalent strain between plies 21–22 at the centre of the beam and take the average of all six measurements. Operated by a feedback signal from the FBG measurements, the prescribed displacement input along with the appurtenant FBG measurement is presented in Figure 8A. Furthermore, the deviation between the displacement input and FBG measurement is available in Figure 8B.

In Figure 8B, multiple violations of the error tolerance are observed. The system reacts by adjusting the position of the actuator in the direction necessary to reduce of the error. The resulting displacement pattern operated within the error tolerance is marked with circles in Figure 8B. The discrepancy between the displacement input and each of the six FBG measurements is presented in Figure 9.

Except FBG 2 and FBG 5, a linear dependent discrepancy between the displacement input and FBG reading is observed in Figure 9. This could indicate an unexpected variation of the inter-ply location of the embedded optical fibre. However, other effects including stress concentrations generated by the support rollers /loading nose and imperfections in the specimen also have an influence. The average time elapsed between each iteration is approx. 3.5 s. Three tests are accomplished on the same test specimen. The number of adjustments, needed to maintain a deviation within the error tolerance for each test is presented in Table 2.

To validate the output from the FBG sensors, six strain gauges are attached to the specimen: three at the top in compression and three at the bottom in tension cf. Figure 3. With the assumption of having a linear variation of the strain in the ply stack thickness (*y*-direction), the measurements from the FBG are compared directly with the strain gauge. This is done by multiplying the strain gauge measurement with the factor *n*, which is the distance from the neutral axis (plies 11–12) to the position of the FBG (plies 21–22) divided by half the beam thickness. A load–strain curve is presented in Figure 10 for specimen 1, including the strain in the FBG and appertaining strain gauge multiplied by an *n* factor of 0.91.

Except SG-3/FBG-3 and SG-1/FBG-1, a small deviation between the FBG and strain gauge is detected. However, a systematic error between the FBG and appurtenant strain gauge is detected for all six cases with a confidence interval of 95%. To accept the hypothesis of having a random error between the FBG and appurtenant strain gauge, the factor *n* is adjusted. The results are presented in Table 3 for five different test specimens.

The empty cells in Table 3 refer to a lack of data due to malfunctioning of strain gauges during testing.

DIC displacement control

Static strain control by DIC is performed to restrict the discrepancy between the displacement input and DIC measurements within a predefined error tolerance. The magnitude of the error tolerance is given on the basis of the measurement uncertainty and repeatability [43] offered by the DIC system. The repeatability is determined from a sample of 100 measurements for each measurement point, acquired under unchanged conditions to have a standard uncertainty of 2.91 μm. The measurement uncertainty is determined as the discrepancy between the displacement measured at a measurement point by the DIC system and a micrometre. With 10 samples equally distributed over a displacement range of 0–6 mm, the measurement uncertainty is 0.01 mm. From the given measurement uncertainty and repeatability, an error tolerance of ±0.01 mm is defined, which is equal to 0.17% of the peak displacement. A displacement input with a triangular waveform is assigned including 91 iterations forming five peaks. The peak-to-peak amplitude of the displacement

doi: 10.1111/str.12089

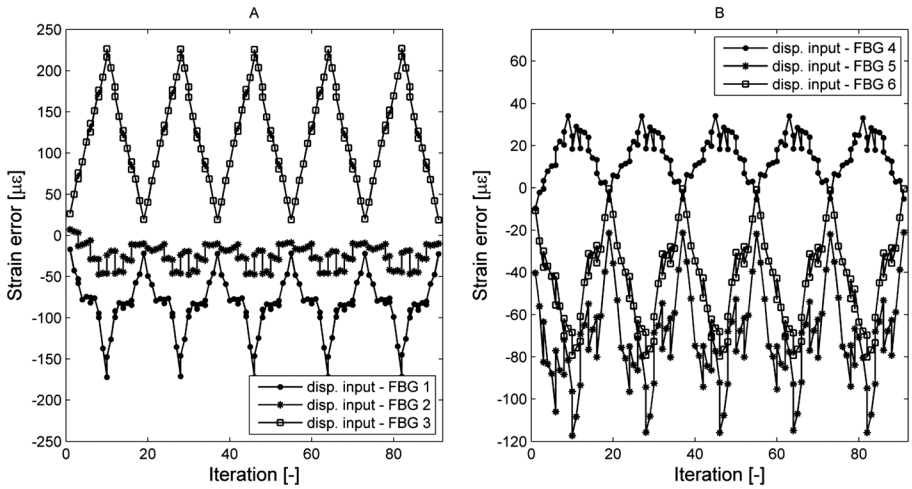

Figure 9: Discrepancy between displacement input and each FBG: (A) FBG 1–3 and (B) FBG 4–6

Table 2: Number of adjustments required in strain control by FBG for each test

Test number (–)	Number of adjustments (–)
1	28
2	26
3	24

input is 5.87 mm at the loading point of the specimen. The displacement input is validated by DIC measurements, which are generated by converting the displacement from each stage point to an equivalent displacement at the loading point and take the average of all three measurements. Operated by a feedback signal from the DIC measurements, the prescribed displacement input along with the appurtenant DIC measurement is presented in Figure 11A. Furthermore, the deviation between the displacement input and DIC measurement is available in Figure 11B.

In Figure 11B, the discrepancy between the displacement input and DIC measurements exceeds the error tolerance multiple times. The system reacts by moving the actuator with a magnitude equal to the respective displacement error. The resulting displacement pattern operated within the error tolerance is marked with circles. The discrepancy between the displacement input and each of the three DIC measurements is presented in Figure 12.

In Figure 12, a linear dependent discrepancy between the displacement input and DIC measurement is observed. The discrepancy increases when enlarging the distance between the loading nose and measurement point in the *x*-direction (see Figure 3). This tendency may be due to the assumptions

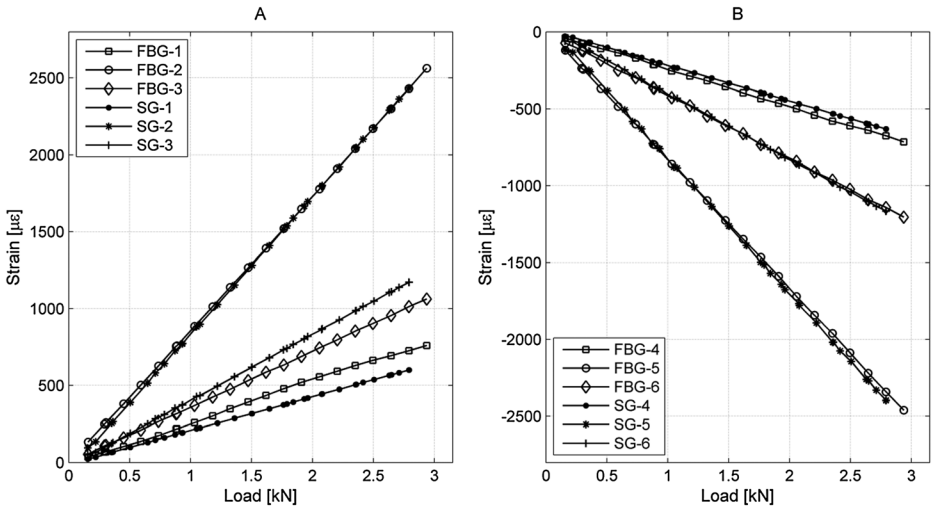

Figure 10: Load–strain curve for each individual FBG and SG: (A) bottom fibres in tension and (B) top fibres in compression

doi: 10.1111/str.12089

Table 3: Factor n to eliminate the deviation between the FBG and appurtenant strain gauge

Test specimen (–)	SG1 (–)	SG2 (–)	SG3 (–)	SG4 (–)	SG5 (–)	SG6 (–)
1	1.01	0.92	0.83	1.14	0.93	0.77
2	0.98	0.93	-	1.00	0.86	0.74
3	1.13	0.89	0.77	0.97	0.87	0.87
4	0.94	-	0.86	0.72	0.79	0.95
5	0.85	-	0.88	1.00	-	0.83

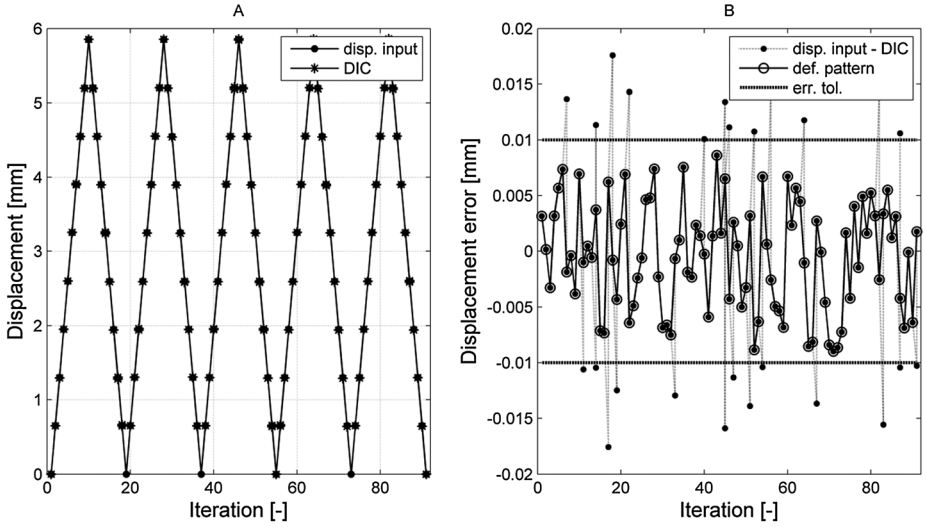

Figure 11: Strain control by DIC: (A) displacement input and DIC and (B) deviation between displacement input and DIC

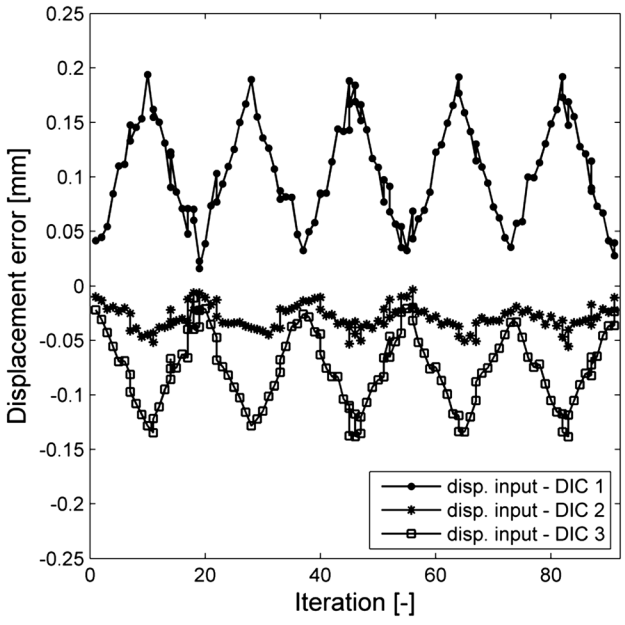

Figure 12: Discrepancy between displacement input and each DIC measurement

concerning the displacement shape of the beam, not being fulfilled. The average time elapsed between each iteration is approx. 3.5 s, and three tests are accomplished on the same test specimen. The number of adjustments needed to maintain a deviation within the error tolerance for each test is presented in Table 4.

Discussion

Control loop

In this investigation, the control loop was successfully demonstrated using two different measurement techniques: FBG and DIC for strain and displacement controls, respectively. Each time the discrepancy between the displacement input and the actual response of the specimen exceeded the error tolerance, the system reacted by moving the actuator with a magnitude equal to the respective displacement error. When the discrepancy was within the error tolerance, the next displacement input was applied in the subsequent iteration.

doi: 10.1111/str.12089

Table 4: Number of adjustments required in displacement control by DIC for each test

Test number (−)	Number of adjustments (−)
1	25
2	17
3	20

The control loop operated with an iteration frequency of 0.29 Hz for the given system, this frequency could be enhanced by using better hardware to operate the control loop. However, changing the system architecture from a state-machine framework to a cascade feedback loop would be another opportunity allowing a full dynamic response of the system [2]. However, given that the sampling rate of the external measurements is lower than the bandwidth of the PID controller, multiple iterations are made without knowing whether the error tolerance is exceeded. This means that, depending on the bandwidth of the external measurement system and PID controller, a number of iterations that are performed between each correlation are executed.

FBG sensor strain control

The control loop was successfully demonstrated for strain control with an error tolerance of $\pm 20\,\mu m\,m^{-1}$, which generated a total of 24–28 correlating adjustments with a total of 91 iterations cf. Figure 8A. According to Figure 8B, it is expected that the number of correlating adjustments is increased if the error tolerance is decreased and vice versa. With a measurement uncertainty and repeatability of $\pm 8.3\,\mu m\,m^{-1}$ and $0.0994\,\mu m\,m^{-1}$, respectively, an error tolerance of $\pm 20\,\mu m\,m^{-1}$ was accepted. However, decreasing the error tolerance to the level of the measurement uncertainty would be an opportunity.

The FBG measurements were compared with strain gauges as a reference, and a systematic error was detected for all six FBGs. This is mainly caused by a combination of two effects: the stress concentrations generated by the support rollers / loading nose and imperfections in the specimen. However, other effects also affect the FBG signal [30]. When comparing the strain acquired by the FBG system with the measurements from the strain gauges, some mismatches are detected cf. Figure 10 and Table 3. This could be explained by stress concentrations along with variations of the distance between the neutral axes to the FBG sensor. However, when $n \geq 1$, cf. Table 3, the FBG sensor appears to be positioned at the same level or above the appurtenant strain gauge. This indicates that the stress concentrations have a significant impact on the FBG measurements rather than variations of the FBG position. To support that theory, previous research with similar specimens showed that the optical fibres were found to be situated at the same inter-ply region [34].

The strain data from the FBG measurement are converted to an equivalent displacement by the Bernoulli–Euler beam theory. An error of that reconstructed displacement will be present due to the number of strain sensors, position of the strain sensors and uncertainty of the strain sensor signal [16]. That error could be erased by calibrating the FBG signal against the surface displacement as a function of the induced forces. However, that solution is only valid when staying within the linear elastic response.

DIC displacement control

The control loop was successfully demonstrated for displacement control with an error tolerance of ±0.01 mm, which generated a total of 17–25 correlating adjustments with a total of 91 iterations, Figure 11. According to Figure 11, it is expected that the number of correlating adjustments is increased if the error tolerance is decreased and vice versa. With a measurement uncertainty and repeatability of 0.01 mm and 2.91 μm, respectively, an error tolerance of ±0.01 mm was selected.

The static displacement control uses three measuring points to reduce the signal noise and the influence of local effects e.g. stresses concentrations, material defects and geometrical imperfections. However, when multiple measurement points are included, it is necessary to make assumptions concerning the displacement shape of the beam that might not be fulfilled. This could be avoided by oversampling a single measurement point, but this approach will only improve the repeatability, not the bias.

In [2], the standard displacement uncertainty is calculated to $\rho_u = 0.0421$ pixels for a facet size of 15 × 15 pixels and shift of 15 pixels. In this study, the standard displacement uncertainty is calculated to 3.3021 μm for a facet size of 15 × 15 pixels and shift of 15 pixels. This is converted to pixels by the measurement height of 330 mm and camera height resolution of 1728 pixels, thereby, 5.236 pixels/mm. With a displacement deviation of 2.91 μm, the resolution is 0.015pixels. This is 2.8 times higher pixel resolution than found in [2].

Conclusion

Five GFRP beams were loaded in the linear elastic regime in a three-point bending test configuration controlled by feedback signals from DIC and FBG measurements for displacement and strain control, respectively, obtained directly on or inside the specimen. The test configuration was obtained using a control loop algorithm, operating

and acquiring data from the servo-hydraulic controller, FBG interrogator and DIC system. It was demonstrated that such a test configuration is beneficial when a given stress state is required as a control parameter in connection with e.g. a complex test rig, loading configuration or specimen geometry. With the precision and accuracy offered by the DIC and FBG system, the test setup was capable of operating within an error tolerance of 0.01 mm and 20 $\mu m\,m^{-1}$ for displacement and strain controls, respectively.

ACKNOWLEDGEMENTS

The authors would like to acknowledge the financial support from the Danish Centre for Composite Structures and Materials (DCCSM) funded by the Danish Council for Strategic Research within Sustainable Energy and Environment (Grant 09-067212).

REFERENCES

1. Mallat, A. and Alliche, A. (2011) A modified tensile test to study the behaviour of cementitious materials. *Strain* **47**, 499–504.
2. Fayolle, X., Galloch, S. and Hild, F. (2007) Controlling testing machines with digital image correlation. *Exp. Tech.* **31**, 57–63.
3. Udd, E. (1996) Fiber optic smart structures. *IEEE* **84**, 60–67.
4. Khoun, L., Oliveira, R. D., Michaud, V. and Hubert, P. (2011) Investigation of process-induced strains development by fibre Bragg grating sensors in resin transfer moulded composites. *Composites* **42**, 274–282.
5. Molimard, J., Vacher, S. and Vautrin, A. (2010) Monitoring LCM Process by FBG sensor under birefringence. *Strain* **47**, 364–373.
6. Hsieh, M. Y., Tsai, L., Chiang, C. C., Lin, C. L. and Fang, B. L. (2012) Curing residual strain monitoring in different layer of Gr/Epoxy laminated composites using embedded optical fiber Bragg grating sensors. *SPIE* **8409**, 1–8.
7. Mitzutani, Y. and Groves, R. M. (2011) Multi-functional measurements using a single FBG sensor. *Exp. Mech.* **51**, 1489–1498.
8. Zhang, H., Ghandehari, M. and Sidelev, A., *et al*. (2011) Monitoring the hysteresis effects in a strain-stress curve of carbon fiber reinforced laminates by FBG technology. *SPIE* **7753**, 1–4.
9. Palaniappan, J., Ogin, S. L., Thorne, A. M., Reed, G. T., Crocombe, A. D., Capell, T. F., Tjin, S. C. and Mohanty, L. (2008) Disbond growth detection in composite–composite single-lap joints using chirped FBG sensors. *Compos. Sci. Technol.* **68**, 2410–2417.
10. Ling, H.-Y., Lau, K.-T., Su, Z. and Wong, E. T.-T. (2007) Monitoring mode II fracture behaviour of composite laminates using embedded fiber-optic sensors. *Composites* **38**, 488–497.
11. Gebremichael, Y. M., Li, W. and Meggitt, B. T., *et al*. (2005) A field deployable, multiplexed Bragg grating sensor system used in an extensive highway bridge monitoring evaluation tests. *IEEE Sens. J.* **5**, 510–519.
12. Kerrouche, A., Boyle, W. J. O., Sun, T., Grattan, K. T. V., Schmidt, J. W., Täljsten, B. (2009) Enhanced FBG sensor-based system performance assessment for monitoring strain along a prestressed CFRP rod in structural monitoring. *Sens. Actuators, A* **151**, 127–132.
13. Kerrouche, A., Boyle, W. J. O., Gebremichael, Y., Sun, T., Grattan, K. T. V., Täljsten, B. and Bennitz, A. (2008) Field tests of fibre Bragg grating sensors incorporated into GFRP for railway bridge strengthening condition monitoring. *Sens. Actuators, A* **148**, 68–74.
14. Gebremichael, Y. M., Li, W. and Boyle, W. J. O., *et al*. (2005) Integration and assessment of fibre Bragg grating sensors in an all-fibre reinforced polymer composite road bridge. *Sens. Actuators, A* **118**, 78–85.
15. Kerrouche, A., Leighton, J., Boyle, W. J. O., Gebremichael, Y. M., Sun, T., Grattan, K. T. V. and Täljsten, B. (2008) Strain measurement on a rail bridge loaded to failure using a fiber Bragg grating-based distributed sensor system. *Sens. Actuators, A* **8**, 2059–2065.
16. Mueller, U. C., Zeh, T., Koch, A. W. and Baier, H. (2006) Fiber optic Bragg grating sensors for high-precision structural deformation control in optical systems. *SPIE* **6167**, 127–132.
17. Guastavino, R. and Göransson, P. (2007) A 3D displacement measurement methodology for anisotropic porous cellular foam materials. *Polym. Test.* **26**, 711–719.
18. Owolabi, G. M. and Singh, M. N. K. (2009) A comparison between two analytical models that approximate notch-root elastic-plastic strain-stress components in two-phase, particle-reinforced, metal matrix composites under multiaxial cyclic loading: experiments. *Int. J. Fatigue* **28**, 918–925.
19. Jones, A., Shaw, J. and Wineman, A. (2006) An experimental facility to measure the chemorheological response of inflated elastomeric membranes at high temperature. *Exp. Mech.* **46**, 579–587.
20. Moser, R. and Lighter, J. G. (2007) Using three-dimensional digital imaging correlation techniques to validate tire finite-element model. *Exp. Tech.* **31**, 29–36.
21. Helm, J. D., Sutton, M. A. and McNeill, S. R. (2003) Deformations in wide, center-notched, thin panels, Part I: three-dimensional shape and deformation measurements by computer vision. *Opt. Eng.* **42**, 1293–1305.
22. Vialettes, P., Siguier, J.-M., Guigue, P., Karama, M., Mistou, S., Dalverny, O., Granier, S. and Petitjean, F. (2006) Experimental and numerical simulation of super-pressure balloon apex section: mechanical behavior in realistic flight conditions. *Adv. Space Res.* **37**, 2077–2081.
23. Leblanc, B., Niezrecki, C., Avitabile, P., Chen, J., Sherwood, J. and Hughes, S. (2011) Full-field inspection of a wind turbine blade using three-dimensional digital image correlation. *SPIE* **7979**, 2077–2081.
24. Luo, P. F. and Huang, F. C. (2000) Application of stereo vision to the study of mixed-mode crack-tip deformations. *Opt. Lasers Eng.* **33**, 349–368.
25. Corr, D., Accardi, M., Graham-Brady, L. and Shah, S. (2007) Digital image correlation analysis of interfacial debonding properties and fracture behavior in concrete. *Eng. Fract. Mech.* **74**, 109–121.
26. Pan, B. and Li, K. (2011) A fast digital image correlation method for deformation measurement. *Opt. Lasers Eng.* **49**, 841–847.

doi: 10.1111/str.12089

27. Siebert, T. and Crompton, M. J. (2010) Application of high digital image correlation for vibration mode shape analysis. In: *Society of the SEM Annual Conference*, Indianapolis, Indiana USA.
28. Siebert, T., Becker, T., Splitthof, K. and Neumann, I. (2007) High-speed digital image correlation: error estimations and applications. *Opt. Eng.* **46**, 51004/1-7.
29. Arora, H., Hooper, P. A. and Dear, J. P. (2011) Dynamic response of full-scale sandwich composite structures subject to air-blast loading. *Composites Part A* **42**, 1651–1662.
30. Chan, T. H., Yu, L., Tam, H. Y., Ni, Y. Q., Liu, S. Y., Chung, W. H. and Cheng, L. K. (2006) Fiber Bragg grating sensors for structural health monitoring of Tsing Ma bridge: background and experimental observation. *Eng. Struct.* **28**, 648–659.
31. Kreuzer, M. (2013) Strain Measurement with Fiber Bragg Grating Sensors. HBM, Darmstadt, Germany
32. Sutton, M. A., Orteu, J.-J. and Schreier, H. W. (2009) Image Correlation for Shape, Motion and Deformation Measurements, Springer, New York, U.S.A.
33. GOM, ARAMIS. (2006) User Manual - Software. GOM, Braunschweig, Germany.
34. Ibsen Photonics. (2009) I-MON E-USB 2.0 Product Specification. Ibsen Photonics A/S, Farum, Denmark.
35. Nielsen, M. W., Wittrup-Schmidt, J., Hattel, J., Høgh, J. H., Waldbjørn, J. P., Andersen, J. and Markussen, T. L. (2014) Life cycle strain monitoring in glass fibre reinforced polymer laminates using embedded fibre Bragg grating sensors from manufacturing to failure. *Composites Materials, to be published* **48**, 365–381.
36. Zenkert, D. and Battley, M. (2006) Composite Lightweight Structures, DK-2800 Kgs. Technical University of Denmark, Lyngby, Denmark
37. Svrcek, W. Y., Mahoney, D. P. and Young, B. R. (2007) Fundamentals of single input-single output systems. In: Fundamentals of Single Input-Single Output Systems in A Real-Time Approach to Process Control. John Wiley & Sons Ltd., Chichester, UK.
38. MTS. (2004) FlexTest SE & GT Digital Servocontrollers. MTS Systems Corporation, Minnesota, U.S.A.
39. MTS. (2009) LabVIEW Programming Libraries: Model 793.00 Software. MTS Systems Corporation, Minnesota, U.S.A.
40. Bitter, R., Mohiuddin, T. and Nawrocki, M. (2001) LabView Advanced Programming Techniques. CRC Press, Boca Rotan, Florida, USA.
41. Ibsen Photonics. (2011) Camera driver manual. Ibsen Photonics A/S, Farum, Denmark.
42. Ibsen Photonics. (2011) User Manual, Ibsen Photonics A/S, Farum, Denmark.
43. GOM. (2006) The GOM Scripting Language. GOM, Braunschweig, Germany.

